

# Issues and opportunities from Peltier effect in functionally-graded colusites: from SPS temperature modeling to enhanced thermoelectric performances

Gabin Guélou,<sup>1</sup> Christophe Couder,<sup>1</sup> Charles Manière,<sup>1</sup> Christophe Candolfi,<sup>2</sup> Bertrand Lenoir,<sup>2</sup> Lucile Lallemand,<sup>3</sup> Christophe Coureau,<sup>3</sup> Emmanuel Guilmeau<sup>1,\*</sup>

<sup>1</sup> Laboratoire CRISMAT, UMR 6508, CNRS, ENSICAEN, 6 Boulevard du Maréchal Juin, 14050 Caen Cedex 04, France

<sup>2</sup> Institut Jean Lamour, UMR 7198 CNRS – Université de Lorraine, 2 allée André Guinier-Campus ARTEM, BP 50840, 54011 Nancy Cedex, France

<sup>3</sup> SOLCERA, ZI N°1 rue de l'industrie, 27000 Evreux, France

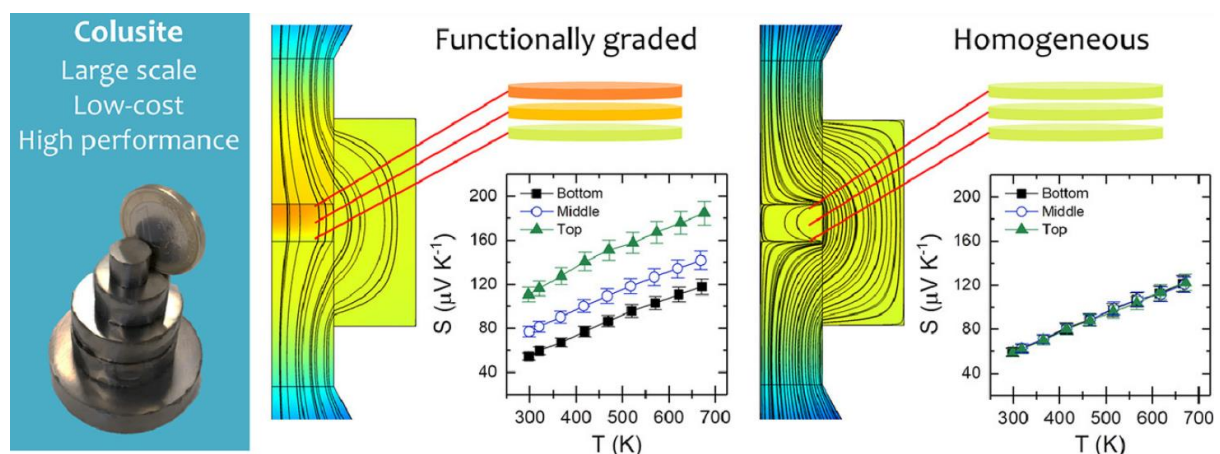
\* Contact author: [emmanuel.guilmeau@ensicaen.fr](mailto:emmanuel.guilmeau@ensicaen.fr)

**Keywords:** thermoelectric, sulfide, colusite, scale up, ball milling

## Abstract

The quaternary sulphide V-Sn colusite,  $\text{Cu}_{26}\text{V}_2\text{Sn}_6\text{S}_{32}$ , is one of the most promising cost-efficient thermoelectric materials to date because of the low toxicity, wide availability and low cost of the composing elements. Recent studies have demonstrated the potential of this environmentally-friendly material and its transport properties are now well understood. In the present work, we take the next step of producing large quantities of optimised V-Sn colusite using industrial-grade precursors and investigating the effect of Spark Plasma Sintering (SPS) in the production of large cylindrical pucks of up to 30 mm in diameter and 10 mm in thickness. In the process, we identified and solved several key issues including the generation of temperature gradients during SPS, porosity and defect formation. The generation of radial and axial temperature gradients within the sample during SPS has been modeled using modified Fourier and Ohm laws and confirmed experimentally thanks to the  $T_{\text{SPS}}$ -dependent transport properties of V-Sn colusite and EDS analysis. We demonstrate that large pucks of colusite with enhanced thermoelectric properties can be produced using a combination of SPS and High-temperature Isostatic Press (HIP). Overall, our work experimentally and theoretically demonstrates that the production of both homogeneous and functionally-graded bulk materials can be easily up-scaled through a careful control of the SPS conditions.

## Graphical Abstract



## 1. Introduction

Thermoelectricity (TE) relies on the ability of optimised materials to generate a potential gradient from a temperature difference high enough so that a TE device can effectively convert a sizeable portion of thermal energy into a useful electrical current. The conversion efficiency of a TE material directly relies on a particular combination of electrical and thermal properties embedded in the dimensionless thermoelectric figure of merit,  $ZT = S^2T/\rho\kappa$ , where  $S$  is the Seebeck coefficient (or thermopower),  $\rho$  is the electrical resistivity and  $\kappa$  is the total thermal conductivity. So far, decades of research, involving a broad range of materials, have seen TE devices restricted to niche applications such as space exploration for which the cost and toxicity combined to the relatively low efficiency of such devices are outweighed by their reliability and lifespan.[1–6] In order to popularise the use of TE devices and significantly contribute to reducing our greenhouse gas emission, the production of large amount of TE materials from low-cost, widely available, non-toxic precursors using cost-effective synthesis and manufacturing techniques is the next milestone.

Amongst the promising families of materials, ternary and quaternary  $n$ - and  $p$ -type copper sulphides stand out by their high performance-to-cost ratio with many of the best performing compositions being free of heavy and toxic elements. This is in particular the case of bornite  $\text{Cu}_5\text{FeS}_4$ ,[7–9], stannoidite  $\text{Cu}_8\text{Fe}_3\text{Sn}_2\text{S}_{12}$ ,[10] germanite derivative  $\text{Cu}_{22}\text{Fe}_8\text{Ge}_4\text{S}_{32}$ ,[11,12] mohite  $\text{Cu}_2\text{SnS}_3$ ,[13] kesterite  $\text{Cu}_2\text{ZnSnS}_4$ ,[14,15]  $\text{Cu}_4\text{Sn}_7\text{S}_{16}$ ,[16] chalcopyrite  $\text{CuFeS}_2$ [17], tetrahedrites  $\text{Cu}_{12-x}\text{T}_x\text{Sb}_4\text{S}_{13}$  ( $T = \text{Mn, Fe, Ni, Zn}$ ).[18–24] and colusites  $\text{Cu}_{26}\text{T}_2\text{M}_6\text{S}_{32}$  ( $T = \text{V, Nb, Ta, Cr, Mo, W; M = Sn, Ge}$ ).[25–31] In our previous works, we reported a figure of merit,  $ZT$ , of 0.9 at 673 K, for the environmentally-friendly V-Sn colusite,  $\text{Cu}_{26}\text{V}_2\text{Sn}_6\text{S}_{32}$ , a highly promising mineral-derivative that rivals the state-of-the-art PbTe-based compounds for mid-temperature range applications in power generation.[32] Such performance was

achieved through careful control over the formation of short-to-medium range structural defects and sulphur loss promoted by the sintering temperature.[28] This enabled the simultaneous optimisation of electrical and thermal properties via charge carrier concentration tuning and thermal conductivity reduction. Following this work, we demonstrated the feasibility of an up-scaled production using industrial binary precursors and large-batch mechanical alloying, while retaining excellent TE properties.[30]

Here, we now turn towards the production of large monoliths of V-Sn colusite using Spark Plasma Sintering (SPS) and address the key issues related to the inhomogeneity of the temperature within the puck during consolidation. A temperature gradient spontaneously forms during current-activated, pressure-assisted densification (CAPAD) because of the Peltier effect.[33,34] This is particularly important in the present case where the sintering temperature is of paramount importance to obtain the desired TE properties.[28] We combined computational Joule heating/thermoelectric modeling and experimental data in order to determine the extent of this issue in V-Sn colusite and to develop a reproducible procedure to cancel the temperature gradient. Of note, promoting a carefully-controlled temperature gradient during sintering may also offer a way of producing functionally-graded materials.[35] Using this optimised procedure, we demonstrate the production of large monoliths of V-Sn colusites with enhanced TE properties.

## **2. Results and discussions**

### *2.1. Modeling of SPS heating affected by Peltier effect*

In a typical SPS configuration using graphite mould and punches, the powdered sample is placed directly between carbon tabs. This allows the electrical current to flow through or around the sample depending on the difference of electrical resistivity between the sample and the mould, as well as on the contact resistance at the junction between the different components of the set-up. In all performing thermoelectric materials like colusite, the

combination of high electrical conductivity and high Seebeck coefficient cannot be ignored when attempting to control the temperature during SPS. This is particularly important as we demonstrated the dramatic impact of temperature over the TE properties of colusite.[28,30] In order to obtain a qualitative map of the temperature distribution in a large consolidated colusite sample, we investigated the multiphysics modeling of SPS Joule heating explicitly taking into account thermoelectric effects. The construction of the Joule heating model and all electric/thermal contact resistance at each SPS interfaces is detailed elsewhere.[36] The thermoelectric effect is added through the Seebeck coefficient, which affects the Joule heating model as described by Maizza *et al.*[33]

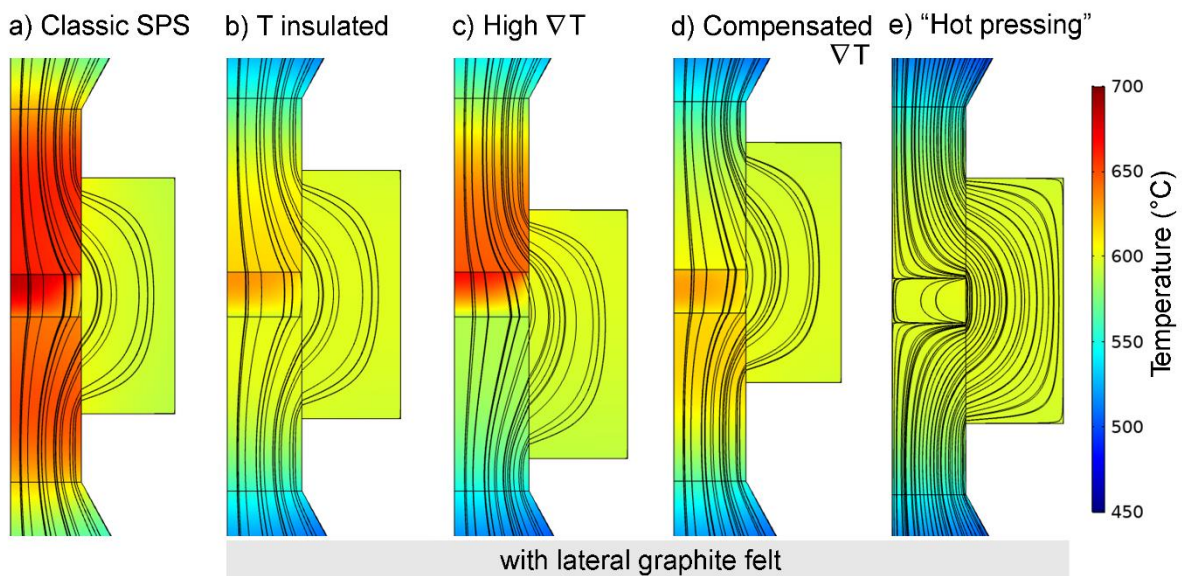


**Figure 1.** Numerical investigation of SPS heating in (a) “typical” SPS configuration, (b,c,d,e) with graphite felt and for special configurations: (c) exaggerating and (d) compensating the specimen temperature gradient by moving the axial die position and (e) electrically insulating the upper and lower powder interfaces (i.e. “hot press” configuration). The solid black streamlines represent the current density flow.

The modeling of heat flux within various configurations of the mould and punches, using the aforementioned simulation, are shown in Figure 1 and S1. A “typical” SPS configuration (Figure 1a) considering the thermoelectric performance of the fully ordered stoichiometric colusite,[28] reveals the generation of two distinct (axial and radial) temperature gradients. The axial component,  $\Delta T_P$ , is a direct consequence of the Peltier effect caused by the relatively high Seebeck coefficient in *p*-type colusite. Because the electrical current flows from bottom to top in the SPS press used in this work, the Peltier effect implies a heat flow from the lower section to the top. Considering the impact of the thermal contact resistance at the upper/lower powder/punch interfaces, these partial thermal barriers tend to reduce the lower punch heat flow (by Peltier effect) and conversely confine the heat at the upper powder interface. Consequently, the horizontal thermal contact resistance exaggerates the Peltier thermal gradient in the powder. Another inhomogeneity in the temperature arises from heat loss through radiation from the mould resulting in a radial temperature difference,  $\Delta T_R$  and an erroneous estimation of the powder temperature from the temperature measured on the die ( $\Delta T_R \sim 75$  K, Figure 1a). In Figure 1a, the temperature difference between the powder/punch column and the mould is clear and worsened by the contact resistance between them. This radial temperature gradient adds up to the axial component and results in an underestimation of the average temperature in the sample area. In order to dispose of these temperature gradients and to monitor the sintering temperature more accurately, we apply two simple corrections that can be easily scaled-up. First, in order to equilibrate the temperature in the punches and the mould, we thermally insulated the latter using a graphite felt. To simulate its impact on heat flux, we assumed a thermal insulation on the lateral die surface (Figure 1b). From this simulation, it appears that, despite the contact resistance, between the punches and mould, the temperature is rather homogeneous across the set-up, with only the Peltier thermal gradient left through the sample remaining. From here, we can either exaggerate this  $\Delta T_P$ , by

displacing the mould downward (Figure 1c), partially compensate it by displacing the mould upward (Figure 1d) or almost cancel it by electrically insulating the upper/lower powder interfaces *via* a boron nitride spray (Figure 1e). Exaggerating  $\Delta T_P$  by moving the die downward (Figure 1c) enables to produce samples with functionally-graded properties so long as these depend on the sintering temperature, as it is the case for the V-Sn colusite. The compensated configuration (Figure 1d) is poorly efficient as the thermal contact resistance still implies the development of  $\Delta T_P \sim 20\text{K}$  despite the higher lower punch temperature. Conversely, the electrically insulated configuration (Figure 1e) forces the current flux out of the sample and through the mould, subsequently cancelling  $\Delta T_P$  in a so-called “hot press” configuration. Note that the temperature fed back to the PID is calculated to be much closer to the temperature experienced by the sample than in the previous configurations (Figure 1a).

In the following sections, the thermoelectric properties of large pucks (30 mm diameter, 10 mm thick) of V-Sn colusite prepared from up-scaled mechanical alloying[30] are discussed. First, we compare the thermoelectric properties of the top, middle and bottom segments between two pucks prepared in either a “typical” SPS (Figure 1a) or “hot press” (Figure 1e) configuration. In a second time, we discuss the density issues related to induced sulphur loss in large samples and demonstrate that an additional High temperature Isostatic Pressing (HIP) is successful in obtaining excellent density and controlled thermoelectric performances.

## *2.2. Experimental confirmation of thermal gradients*

The mechanochemical synthesis of the powders used for the SPS sintering of large samples is described elsewhere.[30] The pre-reacted powders are then allowed to crystallise in-situ during the SPS sintering, forming a range of structural defects that depend on the temperature and sulphur volatilisation. The unit cell parameter,  $a$ , of the sintered material varies significantly with the level of disorder in the crystal structure. With binary sulphide

precursors at low sintering temperature, the unit cell remains at around 10.76 Å with the tendency of forming vanadium-rich core shell microstructure from incomplete crystallisation.[30] The unit cell can be as high as *ca.* 10.83 Å for hot-pressed samples prepared from high purity elements, and containing a large proportion of structural defects.[28] Regardless of the choice of precursors, it appears that high temperature sintering (1023 K – 1083 K) yield the best results with a higher *ZT* value. It is therefore of prime importance to reproduce high-temperature sintering on a larger scale. In order to monitor the temperature experienced by the sample during sintering, and to confirm our theoretical model, we carried out Rietveld refinements of the XRPD data acquired at the top, middle and bottom cross sections of Ø30 mm pucks sintered at 873 K from typical SPS and “hot press” configurations (Table 1, Figure 2 and Figure S2 and S3 of the supplementary information).

**Table 1.** Results from Rietveld refinements from XRPD room temperature data of scaled up sintered colusite  $\text{Cu}_{26}\text{V}_2\text{Sn}_6\text{S}_{32}$ .

		Classic SPS Ø30 - SPS873			"hot press" Ø30 - SPS873		
		Bottom	Middle	Top	Bottom	Middle	Top
	$a$ (Å)	10.7734(2)	10.8083(1)	10.8098(1)	10.7868(1)	10.7851(1)	10.7890(1)
	$R_{wp}$ (%)	8.06	9.54	7.73	9.39	9.05	9.65
	$\chi^2$	2.063	2.025	1.891	2.039	1.825	2.144
	$\rho$ (g cm <sup>-3</sup> )	4.637	4.593	4.591	4.62	4.622	4.617
V	$B_{iso}$ (Å <sup>3</sup> )	4.9(4)	1.5(2)	0.3(1)	2.1(2)	1.9(2)	1.9(2)
Cu(1)	$B_{iso}$ (Å <sup>3</sup> )	1.84(4)	2.17(3)	2.22(2)	1.96(3)	1.55(3)	1.65(3)
	$x$	0.2514(4)	0.2527(3)	0.2539(2)	0.2540(3)	0.2526(3)	0.2529(3)
Cu(2)	$B_{iso}$ (Å <sup>3</sup> )	1.84(4)	2.17(3)	2.22(2)	1.96(3)	1.55(3)	1.65(3)
	$x$	0.2529(6)	0.2535(5)	0.2548(3)	0.2517(8)	0.2529(5)	0.2530(5)
Cu(3)	$B_{iso}$ (Å <sup>3</sup> )	1.84(4)	2.17(3)	2.22(2)	1.96(3)	1.55(3)	1.65(3)
Sn	$B_{iso}$ (Å <sup>3</sup> )	6.4(1)	3.01(5)	2.91(4)	3.93(6)	3.86(7)	4.40(7)
S(1)	$B_{iso}$ (Å <sup>3</sup> )	1.23(5)	1.70(5)	1.81(3)	1.63(4)	1.14(4)	1.36(4)
	$x$	0.1355(6)	0.1318(6)	0.1270(6)	0.1299(7)	0.1324(5)	0.1321(6)
S(2)	$B_{iso}$ (Å <sup>3</sup> )	1.23(5)	1.70(5)	1.81(3)	1.63(4)	1.14(4)	1.36(4)
	$x$	0.3867(4)	0.3798(3)	0.3798(2)	0.3821(3)	0.3835(3)	0.3836(3)
	$y$	0.3655(4)	0.3654(3)	0.3672(3)	0.3659(3)	0.3656(3)	0.3649(3)
	$z$	0.1196(5)	0.1221(6)	0.1243(5)	0.1225(6)	0.1204(5)	0.1216(5)
	Impurities	-	2% Cu <sub>3</sub> VS <sub>4</sub>	-	-	-	-

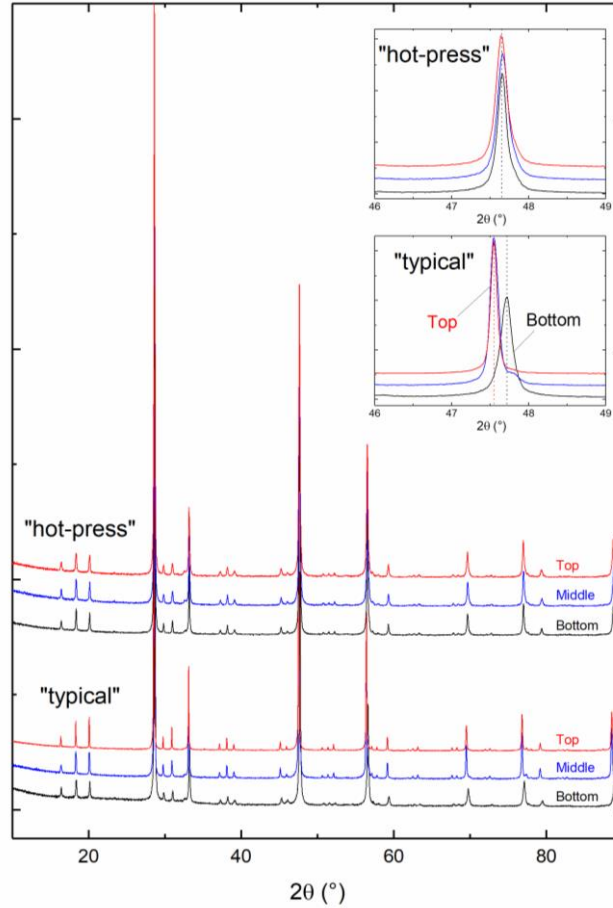


**Figure 2.** XRPD room temperature data of scaled-up sintered colusite  $\text{Cu}_{26}\text{V}_2\text{Sn}_6\text{S}_{32}$  including the top, middle and bottom cross sections in typical and “hot press” configurations. Rietveld refinements are given in the supplementary information (Figure S2 and S3).

As expected from the theoretical model, the sample sintered in a typical SPS configuration shows sign of inhomogeneous temperature with a range of unit cell parameters across the puck, from *ca.* 10.77 Å to *ca.* 10.81 Å, similar to that of the minimum and maximum values observed in lab-scale samples. Conversely, the sample sintered in “hot press” configuration shows a very consistent unit cell parameter within the puck, varying only slightly from 10.7851(1) Å to 10.7898(1) Å, albeit in a non-systematic fashion. These results support our theoretical model owing to the established relationship between unit cell parameter and sintering temperature. This is further confirmed by the measured thermoelectric properties of

the sample (Figure 3 and 4). In the typical SPS configuration, the electrical resistivity, Seebeck coefficient and resulting power factor of up-scaled colusite depend on the position of the measured cross section. The top section, predicted to be experiencing higher temperatures during SPS, exhibits the largest unit cell parameter and the most semiconducting electrical transport properties, with electrical performances close to those of highly-disordered colusite.[28,30,37] As the cross section approaches the bottom part, the transport properties and unit cell parameters are consistent with a progressively more ordered colusite, evidencing a progressively lower effective sintering temperature. The higher sulphur volatilisation occurring as we move closer to the upper punch of the SPS, *i.e.* closer to the top section, can be clearly seen from point-by-point EDX analysis, carried out across the sample every 500  $\mu\text{m}$  (Figure S4). In the top section of the puck, the electrical resistivity displays values ranging between 3.0  $\text{m}\Omega\text{ cm}$  and 4.2  $\text{m}\Omega\text{ cm}$  at 300 K and 700 K, respectively, with the distinctive minimum at around 350 K.[30] Similarly, the Seebeck coefficient is high with values between 110  $\mu\text{V K}^{-1}$  and 185  $\mu\text{V K}^{-1}$  over the investigated temperature range. The electrical transport properties then become increasingly metallic at the middle and bottom sections of the puck with room-temperature electrical resistivity values of 1.5  $\text{m}\Omega\text{ cm}$  and 1.0  $\text{m}\Omega\text{ cm}$ , respectively, up to 2.2  $\text{m}\Omega\text{ cm}$  and 1.7  $\text{m}\Omega\text{ cm}$  at 700 K. Meanwhile, the Seebeck coefficient also decreases from 77  $\mu\text{V K}^{-1}$  and 55  $\mu\text{V K}^{-1}$  at 300 K to 142  $\mu\text{V K}^{-1}$  and 118  $\mu\text{V K}^{-1}$  at 700 K for the middle and bottom sections, respectively. In “hot press” configuration, the variations between the different sections are completely cancelled out and the electrical performances are those of the bottom, *i.e.* the coldest section of the sample in a typical SPS configuration. A similar conclusion can be drawn from the thermal conductivity with very different values measured for the different cross sections in the typical SPS configuration (Figure 4). The top section exhibits thermal conductivity values ranging from 1.54  $\text{W m}^{-1}\text{ K}^{-1}$  to 1.12  $\text{W m}^{-1}\text{ K}^{-1}$  at 300 K and 673 K, respectively, while the top of the puck shows a thermal

conductivity about 35 % lower, consistent with a higher sintering temperature, larger unit cell parameter and higher level of disorder. This is consistent with a more homogeneous and more stoichiometric sample when using the “hot press” configuration. Overall, the peak  $ZT$  value is functionally graded in a typical SPS configuration while the addition of the insulating barriers leads to a large homogeneous puck with a constant  $ZT$  across the sample (Figure 4).

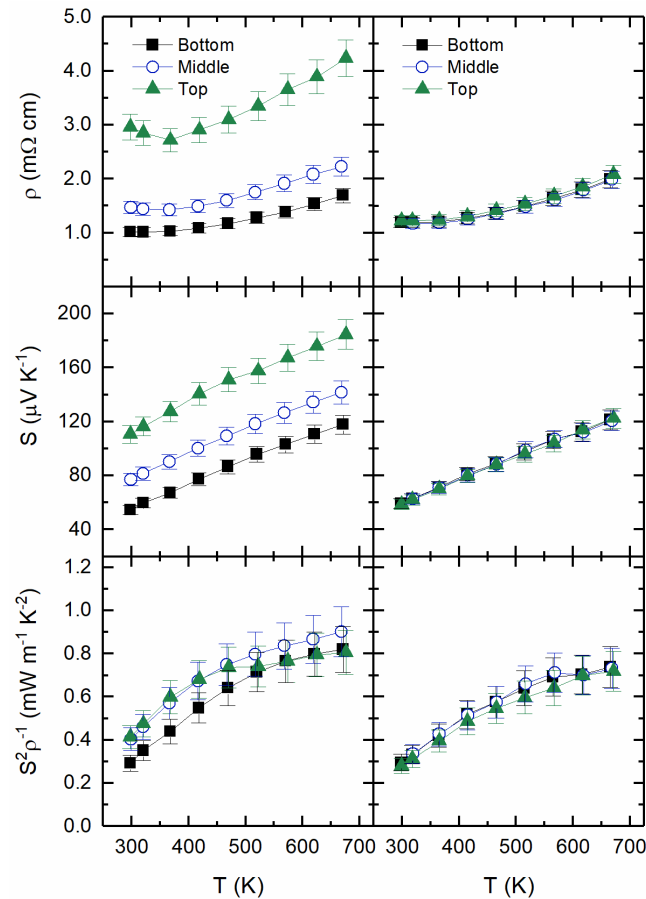


**Figure 3.** Temperature dependence the electrical resistivity, Seebeck coefficient and power factor for  $\text{Cu}_{26}\text{V}_2\text{Sn}_6\text{S}_{32}$  of samples, sintered at 873 K, cut from the bottom, middle and top sections of a 10 mm thick sample ( $\Phi$  30 mm). Left column: in a classic SPS configuration; Right column: in “hot press” configuration (i.e. with insulating spacers and jacket).

Finally, the unit cell parameters and transport properties of V-Sn colusite, sintered at 873 K in “hot press” configuration, are slightly different than those of lab-scale samples, should

they be synthesised from high-purity elements[28] or industrial grade binary precursors.[30] This evidences a discrepancy between the measured temperature in the mould and the actual sintering temperature, confirmed by the electrical transport properties measurements. By comparison, the unit cell parameter and thermoelectric performance of the “hot press” SPS873 sample seem to be consistent with an actual sintering temperature between 1023 K and 1073 K. From our calculations, this seems to suggest that a better thermal insulation of the mould would be needed for better control over the temperature. However, it must be noted that these discrepancies might also arise from differences in sulphur loss and/or defect formation caused by the much lower surface-to-volume ratio in the large pucks. This possibility seems more likely, as evidenced by the expected trend with respect to sintering temperature and the density issues addressed in the following section.

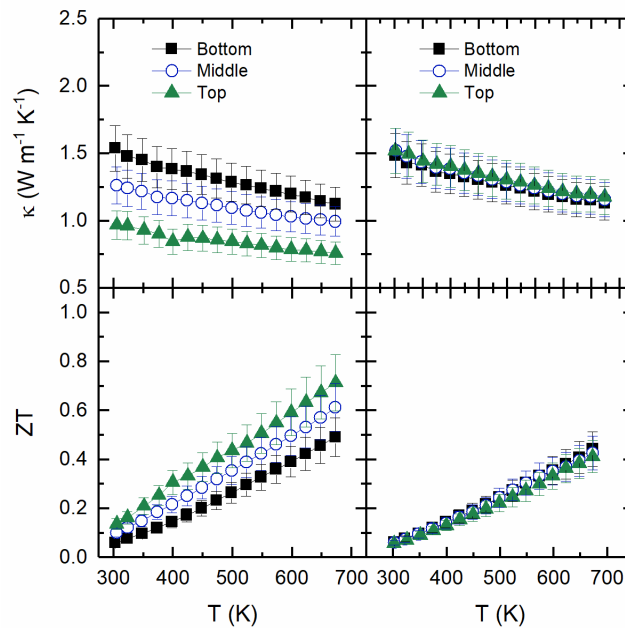


**Figure 4.** Temperature dependence of the thermal conductivity and figure of merit for  $\text{Cu}_{26}\text{V}_2\text{Sn}_6\text{S}_{32}$  of samples cut from the bottom, middle and top sections of a 10 mm thick sample ( $\Phi$  30 mm). Left column: in a classic SPS configuration; Right column: in “hot press” configuration (i.e. with insulating spacers and jacket).

### *2.3. Consolidation and TE optimisation*

As demonstrated previously,[28,30,37] increasing the sintering temperature is crucial to obtaining high thermoelectric performance. We prepared 3 additional pucks of 30 mm in diameter and 10 mm in thickness sintered in the “hot press” configuration, established in the precedent section, at 923 K, 973 K and 1023 K (noted hereafter SPS923, SPS973 and SPS1023, respectively). The differences in surface-to-volume ratio in such large pellets, compared to the  $\varnothing$ 10 mm typically used in lab-scale experiments, led to issues regarding sulphur volatilisation. Indeed, as evidenced by the much lower densities obtained for SPS973 and SPS1023, with closed porosity, it appears that sublimated sulphur remained trapped in the sintered sample and led to high levels of porosity on cooling (Table 2). This is particularly detrimental for higher sintering temperature as attempts to sinter samples at 1073 K led to the formation of millimetre-scale pores within the samples, making them unusable. For samples sintered below 1023 K however, owing to the closed porosity, it was possible to correct for the loss of density by using Hot Isostatic Pressing (HIP). Thus, we produced two additional series including an additional HIP step at 1500 bar and 873 K or 1023 K for 1h. The crossed impact of SPS sintering temperature and HIP temperature on the microstructure and thermoelectric performances has been investigated. Regardless of the HIP temperature, this step was successful in correcting the density, up to 100 % for all samples (Table 2). The measured volume mass even reached values slightly over 100 % of the crystallographic value, the latter being slightly underestimated because of sulphur loss. This is clear from the microstructural analysis (Figure 5 and S5) where pores can be observed in the SPS873 samples while SPS1023 displays more but smaller pores. In both cases, the additional HIP treatment at 873 K is sufficient to obtain an extremely dense material. Aside from the effect on density, the HIP treatments also clearly affect the microstructure of the materials and in particular the concentration and composition of the microstructural defects. In a previous

work, we already established the nature of these defects and the effect of sintering temperature on these defects in smaller SPS samples.[30] We demonstrated that low sintering temperatures led to an incomplete crystallisation of the colusite phase, leaving V-rich core-shell microstructures (CSM) as artefacts of the formation mechanism of colusite. These microstructures progressively disappear to be replaced by a single-phase colusite with regions disordered at the atomic level. The latter observation confirmed the work of Bourgès *et al.* and Suekuni *et al.* on the key role of atomic-scale defects on the thermoelectric performances of colusites.[28,38]

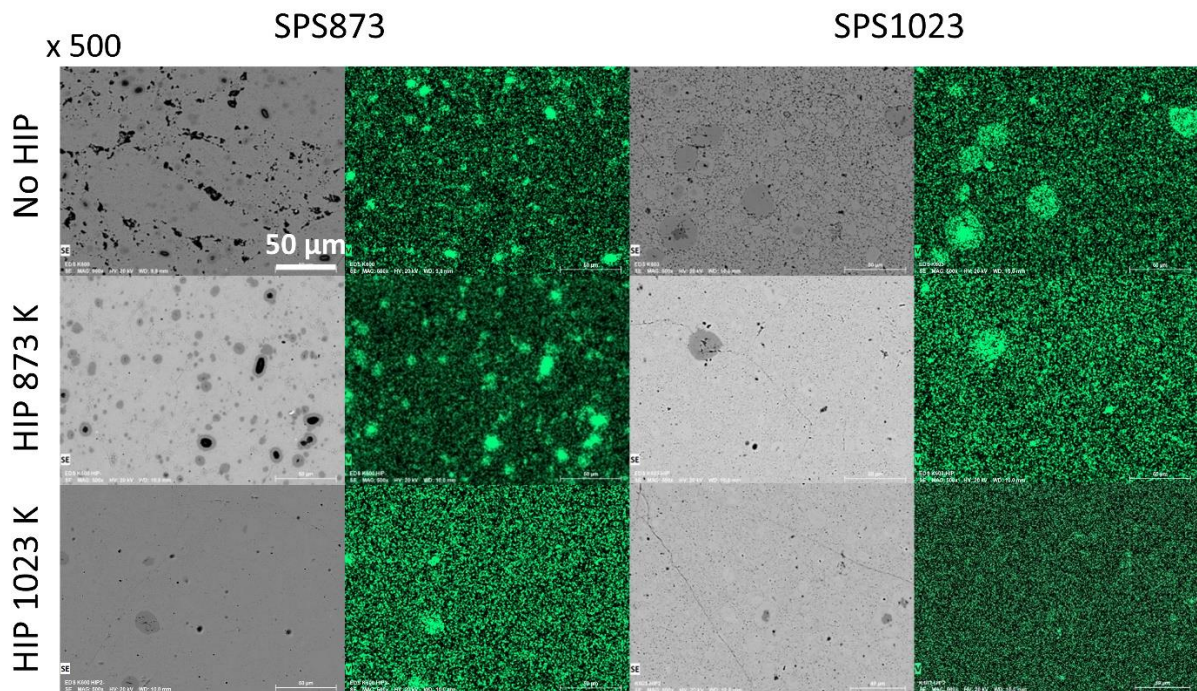


**Figure 5.** Back-scattered scanning electron micrographs ( $\times 500$ ) of polished surfaces of SPS873 and SPS1023 samples and the corresponding V mappings from EDX analysis, before and after HIP at 873 K and 1023 K.

It is thus not surprising to observe a large quantity of V-rich CSM in the SPS873 sample (Figure 5 and 6) while very few could be seen in the SPS1023 sample. However, the latter still exhibits V-rich regions with a composition close to that of colusite with an equal amount

of V and Sn. Interestingly, the observation of the defects in SPS873 and SPS1023 samples with and without HIP treatments evidences a systematic grain growth in V-rich regions, inside the area marked by a beige line. In the SPS873 sample (Figure 6a), the grain size remains small (sub-micron) and homogeneous across the sample, even around the CSM marked by the red and orange lines. After HIP at 873 K, it is clear that the outer layers of the CSM have a significantly larger grain size than the colusite matrix, of around 1  $\mu\text{m}$  (Figure 6b). At the same time, these CSM are scarcer and many have diffused into the colusite matrix leaving V-rich spot-regions without a vanadium metal core. After HIP treatment at 1023 K, the homogeneous grain size within the colusite matrix increases up to 2-3  $\mu\text{m}$  (Figure 6c). However, around the V-rich spot-regions and the few remaining CSM, the grain size can be as much as 5 times larger. A similar observation can be made for the SPS1023 sample where such grain growth, localised around the V-rich regions, can be seen before the HIP treatment (Figure 6d). After HIP at 873 K or 1023 K (Figure 6e and 6f, respectively), nearly all V-rich regions have diffused into the matrix, replaced by spot-regions of large grain sizes dispersed within the colusite matrix. These observations are consistent with the formation mechanism of colusite, through the diffusion of vanadium into a Cu-Sn-S matrix, and highlight the importance of the crystallisation process in shaping the microstructure of colusite materials. At low sintering temperature and without HIP, the materials can be described as a composite of V-poor colusite matrix and V-rich CSM. Previously, in lab-scale experiments, we demonstrated that a complete diffusion process of vanadium and single-phase colusite can be obtained by increasing the sintering temperature.[30] In large consolidated samples however, the associated sulphur volatilisation leads to significant porosity and a HIP treatment is necessary to ensure a high density. In the process, we can clearly observe that the diffusion of vanadium into the colusite matrix is accompanied by a faster grain growth in the regions surrounding a V-rich CSM.

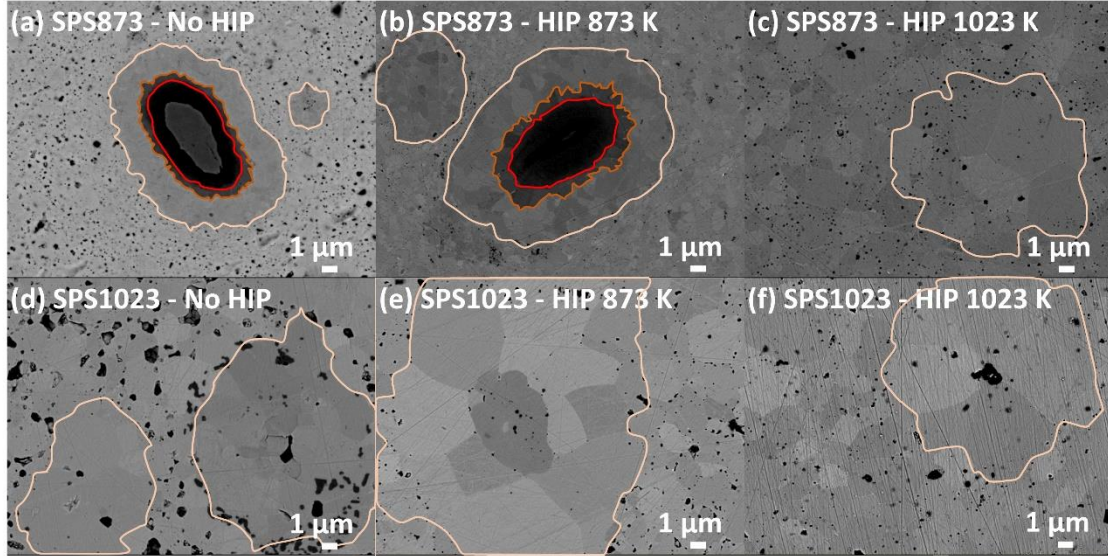


**Figure 6.** Scanning electron micrographs ( $\times 5000$ ) of polished surfaces of SPS873 and SPS1023 samples, before and after HIP at 873 K and 1023 K. The micrographs focus on the characteristic features of the corresponding samples, i.e. V-rich core-shell microstructure (inside the red and orange lines) for SPS873 without and with HIP at 873 K and on the large grain clusters (regions marked by a beige line) in the remaining samples.

**Table 2.** Measured volume mass, relative density and detected impurities for colusite samples sintered at 873 K, 923 K, 973 K and 1023 K, before and after HIP at 873 K and 1023 K.

Sample	$T_{\text{HIP}}$ (K)	$\rho$ ( $\text{g cm}^{-3}$ )	$d$ (%)	Impurities (wt%)
SPS873	-	4.57	99.8	Sulvanite (2.5 %) Vanadium (0.5 %)
SPS923	-	4.52	98.8	Sulvanite (2.2 %)
SPS973	-	4.38	93.0	-
SPS1023	-	4.20	91.3	-
SPS873	873	4.71	102	-
SPS923	873	4.70	102	-
SPS973	873	4.69	102	-
SPS1023	873	4.68	102	-
SPS873	1023	4.64	101	-
SPS923	1023	4.64	101	-
SPS973	1023	4.64	101	-
SPS1023	1023	4.63	101	-

The thermoelectric performances of the three series of samples are shown in Figure S6 and S7. Compared with previous transport property data, the electrical resistivity and Seebeck coefficient for all samples are generally high.[28,30,37] SPS873 is the most metallic sample

with an electrical resistivity varying from 1.46 m $\Omega$  cm to 2.31 m $\Omega$  cm, and a Seebeck coefficient increasing from 65  $\mu$ V K<sup>-1</sup> to 129  $\mu$ V K<sup>-1</sup> at 298 K and 667 K, respectively. This corresponds to a threefold increase compared to the values obtained on smaller sintered pellets. This is likely caused by the differences in the SPS set up and, in particular, by the use of much larger moulds that increase the error in the measurement of the actual temperature experienced by the sample. By comparison with our previous work,[30] and considering that the powders have been prepared in the exact same scaled-up conditions, we can speculate that the temperature in the sample during SPS has been underestimated. However, the presence of a large amount of defects makes it very difficult to estimate the value of the temperature experienced by the sample and a qualitative comparison is more pertinent. Indeed, the observed increase in electrical resistivity and Seebeck coefficient with increasing sintering temperature is consistent with a decrease in the charge carrier concentration through sulphur volatilisation and the complete crystallisation of the colusite phase. This effect becomes nearly negligible for the samples with a HIP treatment at 1023 K. The samples prepared by SPS at temperatures higher than 973 K, without HIP, exhibit an electrical resistivity higher than expected with respect to the Seebeck coefficient, consistent with the low relative density observed for these samples. This issue has been fully eliminated by the additional HIP step, regardless of its temperature. Because the decrease in charge carrier concentration leads to an increased electrical resistivity and Seebeck coefficient, the power factor remains remarkably similar for all samples with high densities. Overall, the best performing sample is SPS923 followed by a HIP step at 1023 K (Figure 7 and 8), although all samples with this HIP temperature have reasonably similar thermoelectric performances (Figure S6 and S7). The SPS873 and SPS923 samples already exhibited high relative density; therefore, the HIP step at 873 K had virtually no impact on the transport properties. However, for samples sintered by SPS at higher temperature, *i.e.* exhibiting a lower relative density after SPS, this HIP at

873 K was successful in increasing the relative density, thus decreasing the electrical resistivity, retaining a high Seebeck coefficient and increasing the thermal conductivity. As a result, these differences arising from the various sintering temperatures are retained and the electrical transport behaviour is increasingly semiconducting with increasing SPS temperature.

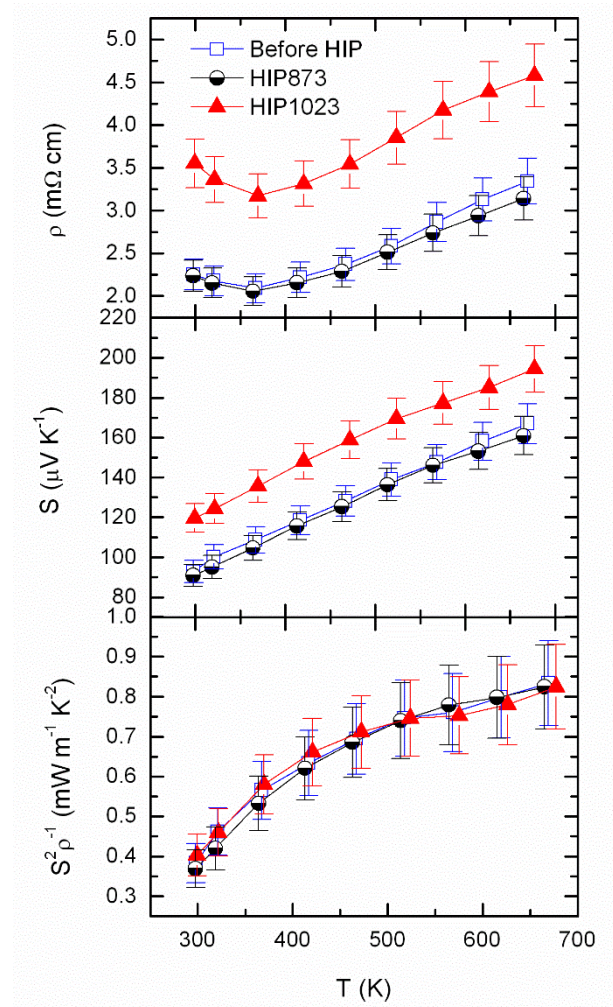


**Figure 7.** Temperature dependence the electrical resistivity, Seebeck coefficient and power factor for  $\text{Cu}_{26}\text{V}_2\text{Sn}_6\text{S}_{32}$  sintered at 923 K in “hot press” configuration (i.e. with insulating spacers and jacket), before and after HIP at 873 K and 1023 K.

The impact of the HIP step at 1023 K, however, is expected to be much more pronounced for all samples and to nearly fully suppress the differences made by the SPS temperature. This is

consistent with previous studies where it was determined that high temperatures lead to sulphur volatilisation and the formation of atomic-scale defects.[28,30,37,38] Regardless of the SPS temperature, a HIP step at 1023 K ensured high density, complete crystallisation of the colusite phase and the removal of most microscale defects. In the same time, as extensively investigated previously, [28,30,37,38] the high temperature leads to the formation of atomic-scale defects that ultimately reduce the thermal conductivity. This is clear from the significant decrease measured for SPS923 + HIP at 1023 K (Figure 8) from  $1.04 \text{ W m}^{-1} \text{ K}^{-1}$  to  $0.81 \text{ W m}^{-1} \text{ K}^{-1}$  at 300 K and from  $0.86 \text{ W m}^{-1} \text{ K}^{-1}$  to  $0.65 \text{ W m}^{-1} \text{ K}^{-1}$  at 673 K. This reduction occurs while the power factor (Figure 7) remains high and unchanged compared to before and after HIP at 873 K. A maximum value of  $0.83 \text{ mW m}^{-1} \text{ K}^{-2}$  is obtained for all three samples as a result of the simultaneous increase in electrical resistivity and Seebeck coefficient. This evidences a decrease in charge carrier concentration caused by the highest level of sulphur loss induced by the HIP step at 1023 K. Data for the remaining samples are given in the supplementary information (Figure S6 and S7).

As a result, while all samples subjected to a HIP step at 1023 K reached a maximum  $ZT$  value of around 0.75 at 673 K, the best performance was achieved for the SPS923 sample with  $ZT = 0.85$  at 673 K. These results both confirm the need for high temperature in order to improve the performances of the V-Sn colusite and the nonessential nature of a high temperature sintering step, so long as it is followed by an annealing process such as HIP. The fact that SPS923, after HIP at 1023 K, exhibits the highest  $ZT$  most likely depends on the type of disorder already present in the sample before annealing. Indeed, this sample still showed significant levels of microstructural defects, illustrated by detectable amounts of sylvanite in the XRPD pattern. For samples sintered at 973 K and 1023 K, the issue related to density and the high level of sulphur volatilisation might play a role in the performance after the HIP

step. In these two samples, the charge carrier concentration has been exceedingly reduced, leading to a lower power factor and ultimately lower  $ZT$ .

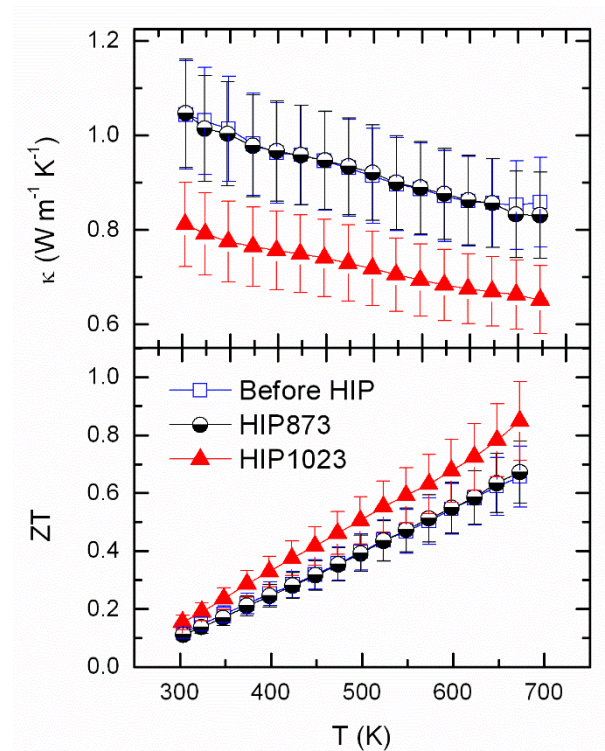


**Figure 8.** Temperature dependence of the thermal conductivity and figure of merit for  $\text{Cu}_{26}\text{V}_2\text{Sn}_6\text{S}_{32}$  sintered at 923 K in “hot press” configuration (i.e. with insulating spacers and jacket), before and after HIP at 873 K and 1023 K.

### 3. Conclusion

The production of large cylindrical pucks of industrial-grade colusite,  $\text{Cu}_{26}\text{V}_2\text{Sn}_6\text{S}_{32}$ , using 100g scale mechanical alloying and spark plasma sintering has been successfully demonstrated. In the process, several issues related to the formation of temperature gradients in the sample during SPS have been successfully modeled, experimentally confirmed and easily prevented by adding insulating barriers forcing the current out of the sample area. It was previously established that optimising the thermoelectric properties of V-Sn colusite required temperature-induced disorder, in particular atomic-scale defects promoted by high

temperatures. In this scaled-up process, producing pucks of 30 mm in diameter and 10 mm in thickness, we evidenced new issues related to in-situ sulphur volatilisation, leading to a low relative density and a lower TE performance. We demonstrated that an additional HIP step at 873 K was sufficient in correcting this density issue; however, a higher temperature of 1023 K yields better results directly from samples sintered at lower SPS temperatures. Overall, the best performing sample, sintered at 923 K and subjected to HIP at 1023 K, exhibits a peak  $ZT$  of 0.85 at 673 K. This value is on par with the best lab-scale high-purity V-Sn colusite reported to date and can be obtained in very large amounts. Finally, this approach can be of interest for a wide range of applications involving Spark Plasma Sintering. These include the optimisation of TE materials and applications that will benefit from obtaining functionally-graded materials.

## **4. Experimental Section**

### *4.1. Synthesis and consolidation*

Polycrystalline samples of  $\text{Cu}_{26}\text{V}_2\text{Sn}_6\text{S}_{32}$  were synthesized by mechanical alloying using industrial-grade binary precursors SnS and CuS (Tribotecn) and V (99.9%, Alfa Aesar). Large batches of products (100g) were obtained from the ball-milling of the precursors in a 250 ml tungsten carbide jar containing 15 balls of 20 mm under argon atmosphere. This was carried out in a Fritsch Pulverisette 5 Premium line planetary ball-mill operating at room temperature. The stoichiometric mixture of precursors was milled for a total of 12 h at 400 rpm in sequences of 30 min with 5 min intervals. The obtained powders were then loaded in graphite dies of 30 mm in diameter and densified by spark plasma sintering in a SPS-FCT HPD 25. The different sintering temperatures have been selected by considering previously reported TGA/DSC analysis and adapted following the difficulties encountered during the scale up procedure.[30] Regardless of the sintering temperature, heating and cooling rates of respectively  $50 \text{ K min}^{-1}$  and  $20 \text{ K min}^{-1}$  were used with a 30 min isotherm at the sintering

temperature under a pressure of 64 MPa. All milling were carried out in inert atmosphere (argon) but storage and manipulation of the precursors and the products of mechanical alloying were done in air. All samples appear to be stable in air.

#### *4.2. Heating simulation*

The calculations of SPS Joule heating were performed by finite-element analyses using the software COMSOL Multiphysics. The governing equations of Joule heating with thermoelectric effect, the electro-thermal boundary conditions, and the graphite and electrothermal contact resistance are described elsewhere. [33,36,39]

#### *4.3. Electrical and thermal properties measurements.*

The electrical resistivity ( $\rho$ ) and Seebeck coefficient ( $S$ ) were measured simultaneously on bar-shaped samples, cut from the obtained SPS samples (as described in the main text), from 300 K up to 700 K on heating and cooling using an ULVAC-ZEM3 instrument under partial helium pressure. A NETZSCH LFA-457 instrument was used for the measurement of the thermal diffusivity under argon flow. The thermal conductivity ( $\kappa$ ) was determined as the product of the geometrical density (confirmed by Archimedes' method), thermal diffusivity, and theoretical heat capacity using the Dulong–Petit approximation. The lattice contribution to the thermal conductivity ( $\kappa_L$ ) was determined by subtracting the estimated electronic component ( $\kappa_e$ ) from the measured total thermal conductivity ( $\kappa$ ). The estimated measurement uncertainties are 6% for the Seebeck coefficient, 8% for the electrical resistivity, 11% for the thermal conductivity, and 16% for the final figure of merit,  $ZT$ . [40]

#### *4.4. X-ray powder diffraction*

Rapid acquisition of X-ray powder diffraction (XRPD) were carried out on reactive powders (before SPS) using two X'PERT Pro MPD PANalytical (Phillips) equipped with a Cu ( $K\alpha_1 = 1.5406 \text{ \AA}$  and  $K\alpha_2 = 1.5444 \text{ \AA}$ ) anticathode. The source was fitted with a PIXcel3D detector

and a nickel filter to eliminate  $K_{\beta}$  copper radiation. High-resolution X-ray powder diffraction (XRPD) data were collected at room temperature using a Bruker D8 Advance Vario 1 two-circle diffractometer ( $\theta$ - $2\theta$  Bragg-Brentano mode) using Cu  $K\alpha$  radiation ( $\lambda = 1.5406 \text{ \AA}$ ) with a Ge (111) monochromator (Johansson type) and a Lynx Eye detector. The XRPD data analyses were performed by Rietveld refinement using the GSAS and ExpGUI software packages.[41,42] Background contribution to the XRPD patterns were estimated manually. Zero-point shift, peak shape parameters, asymmetry parameters, lattice parameters, fractional atomic coordinates and isotropic displacement parameters (*i.e.* Debye-Waller factors  $B_{iso}$ ) were refined.

### **Supplementary Information**

The Supplementary Information is available at DOI:

Figures S1–S7;

### **Author Information**

The authors declare no conflict of interest.

### **Acknowledgements**

The authors would like to thank Christelle Bilot and Jérôme Lecourt for technical support. This work was supported by the French Agence Nationale de la Recherche (ANR) through the programs Energy Challenge for Secure, Clean and Efficient Energy (Challenge 2, 2015, ANR-15-CE05-0027), FEDER and Normandy Region. The authors would like to extend their thanks to Tribotecn for supplying large amounts of industrial grade precursors.

### **References**

- [1] J. He, T.M. Tritt, Advances in thermoelectric materials research: Looking back and moving forward, *Science* (80-. ). 357 (2017) eaak9997. <https://doi.org/10.1126/science.aak9997>.
- [2] G.J. Snyder, S. Toberer, Complex thermoelectric materials, *Nat. Mater.* 7 (2008) 105–114. <https://doi.org/10.1038/nmat2090>.
- [3] D.M. Rowe, Thermoelectrics, an environmentally-friendly source of electrical power, *Renew. Ener.* 16 (1999) 1251–1256.

- [4] J.R. Sootsman, D.Y. Chung, M.G. Kanatzidis, New and old concepts in thermoelectric materials, *Angew. Chemie - Int. Ed.* 48 (2009) 8616–8639. <https://doi.org/10.1002/anie.200900598>.
- [5] G. Min, D.M. Rowe, Chapter 38. Peltier Devices as Generators, in: D.M. Rowe (Ed.), *CRC Handb. Thermoelectr.*, CRC Press, 1995.
- [6] D. Champier, Thermoelectric generators: A review of applications, *Energy Convers. Manag.* 140 (2017) 167–181. <https://doi.org/https://doi.org/10.1016/j.enconman.2017.02.070>.
- [7] P. Qiu, T. Zhang, Y. Qiu, X. Shi, L. Chen, Sulfide bornite thermoelectric material: A natural mineral with ultralow thermal conductivity, *Energy Environ. Sci.* 7 (2014) 4000–4006. <https://doi.org/10.1039/c4ee02428a>.
- [8] G. Guélou, A.V. Powell, P. Vaqueiro, Ball milling as an effective route for the preparation of doped bornite: Synthesis, stability and thermoelectric properties, *J. Mater. Chem. C.* 3 (2015) 10624–10629. <https://doi.org/10.1039/c5tc01704a>.
- [9] V. Pavan Kumar, T. Barbier, P. Lemoine, B. Raveau, V. Nassif, E. Guilmeau, The crucial role of selenium for sulphur substitution in the structural transitions and thermoelectric properties of Cu<sub>5</sub>FeS<sub>4</sub> bornite, *Dalt. Trans.* 46 (2017) 2174–2183. <https://doi.org/10.1039/c6dt04204j>.
- [10] V. Pavan Kumar, T. Barbier, V. Caignaert, B. Raveau, R. Daou, B. Malaman, G. Le Caër, P. Lemoine, E. Guilmeau, Copper Hyper-Stoichiometry: The Key for the Optimization of Thermoelectric Properties in Stannoidite Cu<sub>8+x</sub>Fe<sub>3-x</sub>Sn<sub>2</sub>S<sub>12</sub>, *J. Phys. Chem. C.* 121 (2017) 16454–16461. <https://doi.org/10.1021/acs.jpcc.7b02068>.
- [11] V. Pavan Kumar, L. Paradis-Fortin, P. Lemoine, V. Caignaert, B. Raveau, B. Malaman, G. Le Caër, S. Cordier, E. Guilmeau, Designing a Thermoelectric Copper-Rich Sulfide from a Natural Mineral: Synthetic Germanite Cu<sub>22</sub>Fe<sub>8</sub>Ge<sub>4</sub>S<sub>32</sub>, *Inorg. Chem.* 56 (2017) 13376–13381. <https://doi.org/10.1021/acs.inorgchem.7b02128>.
- [12] V. Pavan Kumar, L. Paradis-Fortin, P. Lemoine, G. Le Caer, B. Malaman, P. Boullay, B. Raveau, G. Guélou, E. Guilmeau, Crossover from germanite to renierite-type structures in Cu<sub>22-x</sub>Zn<sub>x</sub>Fe<sub>8</sub>Ge<sub>4</sub>S<sub>32</sub> thermoelectric sulfides, *ACS Appl. Energy Mater.* 2 (2019) 7679–7689. <https://doi.org/https://doi.org/10.1021/acsami.0c00094>.
- [13] Y. Shen, C. Li, R. Huang, R. Tian, Y. Ye, L. Pan, K. Koumoto, R. Zhang, C. Wan, Y. Wang, Eco-friendly p-type Cu<sub>2</sub>SnS<sub>3</sub> thermoelectric material: crystal structure and transport properties, *Sci. Rep.* 6 (2016) 32501. <https://doi.org/https://doi.org/10.1038/srep32501>.
- [14] M.L. Liu, F.Q. Huang, L.D. Chen, I.W. Chen, A wide-band-gap p-type thermoelectric material based on quaternary chalcogenides of Cu<sub>2</sub>ZnSnQ<sub>4</sub> (Q=S,Se), *Appl. Phys. Lett.* 94 (2009) 202103. <https://doi.org/https://doi.org/10.1063/1.3130718>.
- [15] H. Yang, L.A. Jauregui, G. Zhang, Y.P. Chen, Y. Wu, Nontoxic and abundant copper zinc tin sulfide nanocrystals for potential high-temperature thermoelectric energy harvesting, *Nano Lett.* 12 (2012) 540–545. <https://doi.org/10.1021/nl201718z>.
- [16] C. Bourgès, P. Lemoine, O.I. Lebedev, R. Daou, V. Hardy, B. Malaman, E. Guilmeau, Low thermal conductivity in ternary Cu<sub>4</sub>Sn<sub>7</sub>S<sub>16</sub> compound, *Acta Mater.* 97 (2015) 180–190. <https://doi.org/https://doi.org/10.1016/j.actamat.2015.06.046>.

- [17] D. Chen, Y. Zhao, Y. Chen, T. Lu, Y. Wang, J. Zhou, Z. Liang, Thermoelectric Enhancement of Ternary Copper Chalcogenide Nanocrystals by Magnetic Nickel Doping, *Adv. Electron. Mater.* 2 (2016) 1500473. <https://doi.org/10.1002/aelm.201500473>.
- [18] X. Lu, D.T. Morelli, Y. Xia, F. Zhou, V. Ozolins, H. Chi, X. Zhou, C. Uher, High performance thermoelectricity in earth-abundant compounds based on natural mineral tetrahedrites, *Adv. Energy Mater.* 3 (2013) 342–348. <https://doi.org/10.1002/aenm.201200650>.
- [19] K. Suekuni, K. Tsuruta, T. Ariga, M. Koyano, Thermoelectric properties of mineral tetrahedrites Cu<sub>10</sub>Tr<sub>2</sub>Sb<sub>4</sub>S<sub>13</sub> with low thermal conductivity, *Appl. Phys. Express.* 5 (2012) 2–5. <https://doi.org/10.1143/APEX.5.051201>.
- [20] K. Suekuni, K. Tsuruta, M. Kunii, H. Nishiate, E. Nishibori, S. Maki, M. Ohta, A. Yamamoto, M. Koyano, High-performance thermoelectric mineral Cu<sub>12-x</sub>NixSb<sub>4</sub>S<sub>13</sub> tetrahedrite, *J. Appl. Phys.* 113 (2013) 043712. <https://doi.org/10.1063/1.4789389>.
- [21] Y. Bouyrie, C. Candolfi, V. Ohorodniichuk, B. Malaman, A. Dauscher, J. Tobola, B. Lenoir, Crystal structure, electronic band structure and high-temperature thermoelectric properties of Te-substituted tetrahedrites Cu<sub>12</sub>Sb<sub>4-x</sub>TeX<sub>13</sub> (0.5 ≤ x ≤ 2.0), *J. Mater. Chem. C.* 3 (2015) 10476–10487. <https://doi.org/10.1039/c5tc01636c>.
- [22] R. Chetty, A. Bali, R.C. Mallik, Tetrahedrites as thermoelectric materials: An overview, *J. Mater. Chem. C.* 3 (2015) 12364–12378. <https://doi.org/10.1039/c5tc02537k>.
- [23] T. Barbier, P. Lemoine, S. Gascoin, O.I. Lebedev, A. Kaltzoglou, P. Vaqueiro, A. V. Powell, R.I. Smith, E. Guilmeau, Structural stability of the synthetic thermoelectric ternary and nickel-substituted tetrahedrite phases, *J. Alloys Compd.* 634 (2015) 253–262. <https://doi.org/10.1016/j.jallcom.2015.02.045>.
- [24] T. Barbier, S. Rollin-Martinet, P. Lemoine, F. Gascoin, A. Kaltzoglou, P. Vaqueiro, A. V. Powell, E. Guilmeau, Thermoelectric Materials: A New Rapid Synthesis Process for Nontoxic and High-Performance Tetrahedrite Compounds, *J. Am. Ceram. Soc.* 99 (2016) 51–56. <https://doi.org/10.1111/jace.13838>.
- [25] K. Suekuni, F.S. Kim, H. Nishiate, M. Ohta, H.I. Tanaka, T. Takabatake, High-performance thermoelectric minerals: Colusites Cu<sub>26</sub>V<sub>2</sub>M<sub>6</sub>S<sub>32</sub> (M = Ge, Sn), *Appl. Phys. Lett.* 105 (2014) 132107. <https://doi.org/10.1063/1.4896998>.
- [26] K. Suekuni, F.S. Kim, T. Takabatake, Tunable electronic properties and low thermal conductivity in synthetic colusites Cu<sub>26-x</sub>ZnxV<sub>2</sub>M<sub>6</sub>S<sub>32</sub> (x ≤ 4, M = Ge, Sn), *J. Appl. Phys.* 116 (2014) 063706. <https://doi.org/10.1063/1.4892593>.
- [27] C. Bourgès, M. Gilmas, P. Lemoine, N.E. Mordvinova, O.I. Lebedev, E. Hug, V. Nassif, B. Malaman, R. Daou, E. Guilmeau, Structural analysis and thermoelectric properties of mechanically alloyed colusites, *J. Mater. Chem. C.* 4 (2016) 7455–7463. <https://doi.org/10.1039/C6TC02301K>.
- [28] C. Bourgès, Y. Bouyrie, A.R. Supka, R. Al Rahal Al Orabi, P. Lemoine, O.I. Lebedev, M. Ohta, K. Suekuni, V. Nassif, V. Hardy, R. Daou, Y. Miyazaki, M. Fornari, E. Guilmeau, High-Performance Thermoelectric Bulk Colusite by Process Controlled Structural Disorder, *J. Am. Chem. Soc.* 140 (2018) 2186–2195. <https://doi.org/10.1021/jacs.7b11224>.
- [29] V. Pavan Kumar, A.R. Supka, P. Lemoine, O.I. Lebedev, B. Raveau, K. Suekuni, V. Nassif, R. Al

- Rahal Al Orabi, M. Fornari, E. Guilmeau, High Power Factors of Thermoelectric Colusites Cu<sub>26</sub>T<sub>2</sub>Ge<sub>6</sub>S<sub>32</sub> (T = Cr, Mo, W): Toward Functionalization of the Conductive “Cu–S” Network, *Adv. Energy Mater.* 9 (2019) 1803249. <https://doi.org/10.1002/aenm.201803249>.
- [30] G. Guélou, C. Couder, A. Bourhim, O.I. Lebedev, N. Daneu, F. Appert, J. Juraszek, P. Lemoine, L. Segreto, E. Guilmeau, A scalable synthesis route for multiscale defect engineering in the sustainable thermoelectric quaternary sulfide Cu<sub>26</sub>V<sub>2</sub>Sn<sub>6</sub>S<sub>32</sub>, *Acta Mater.* 195 (2020) 229–239. <https://doi.org/https://doi.org/10.1016/j.actamat.2020.05.039>.
- [31] V. Pavan Kumar, G. Guélou, P. Lemoine, B. Raveau, A. Supka, R. Al Rahal Al Orabi, M. Fornari, K. Suekuni, E. Guilmeau, Copper-rich thermoelectric sulfides: size mismatch effect and chemical disorder in the [TS<sub>4</sub>]Cu<sub>6</sub> complexes of Cu<sub>26</sub>T<sub>2</sub>Ge<sub>6</sub>S<sub>32</sub> (T = Cr, Mo, W) colusites, *Angew. Chemie Int. Ed.* 58 (2019) 15455–15463. <https://doi.org/10.1002/anie.201908579>.
- [32] X.-L.L. Shi, J. Zou, Z.-G.G. Chen, Advanced Thermoelectric Design: From Materials and Structures to Devices, *Chem. Rev.* 120 (2020) 7399–7515. <https://doi.org/10.1021/acs.chemrev.0c00026>.
- [33] G. Maizza, G.D. Mastrorillo, S. Grasso, H. Ning, M.J. Reece, Peltier effect during spark plasma sintering (SPS) of thermoelectric materials, *J. Mater. Sci.* 52 (2017) 10341–10352. <https://doi.org/10.1007/s10853-017-1188-1>.
- [34] A. Becker, S. Angst, A. Schmitz, M. Engenhorst, J. Stoetzel, D. Gautam, H. Wiggers, D.E. Wolf, G. Schierning, R. Schmechel, The effect of Peltier heat during current activated densification, *Appl. Phys. Lett.* 101 (2012) 13113. <https://doi.org/10.1063/1.4731272>.
- [35] O. Guillon, J. Gonzalez-Julian, B. Dargatz, T. Kessel, G. Schierning, J. Räthel, M. Herrmann, Field-Assisted Sintering Technology/Spark Plasma Sintering: Mechanisms, Materials, and Technology Developments, *Adv. Eng. Mater.* 16 (2014) 830–849. <https://doi.org/https://doi.org/10.1002/adem.201300409>.
- [36] C. Manière, L. Durand, E. Brisson, H. Desplats, P. Carré, P. Rogeon, C. Estournès, Contact resistances in spark plasma sintering: From in-situ and ex-situ determinations to an extended model for the scale up of the process, *J. Eur. Ceram. Soc.* 37 (2017) 1593–1605. <https://doi.org/https://doi.org/10.1016/j.jeurceramsoc.2016.12.010>.
- [37] C. Candolfi, G. Guélou, C. Bourgès, A.R. Supka, R. Al Rahal Al Orabi, M. Fornari, B. Malaman, G. Le Caër, P. Lemoine, V. Hardy, J.-M. Zanotti, R. Chetty, M. Ohta, K. Suekuni, E. Guilmeau, Disorder-driven glasslike thermal conductivity in colusite Cu<sub>26</sub>V<sub>2</sub>Sn<sub>6</sub>S<sub>32</sub> investigated by Mössbauer spectroscopy and inelastic neutron scattering, *Phys. Rev. Mater.* 4 (2020) 25404. <https://doi.org/10.1103/PhysRevMaterials.4.025404>.
- [38] K. Suekuni, Y. Shimizu, E. Nishibori, H. Kasai, H. Saito, D. Yoshimoto, K. Hashikuni, Y. Bouyrie, R. Chetty, M. Ohta, E. Guilmeau, T. Takabatake, K. Watanabe, M. Ohtaki, Atomic-Scale Phonon Scatterers in Thermoelectric Colusites with a Tetrahedral Framework Structure, *J. Mater. Chem. A* 7 (2019) 228–235. <https://doi.org/10.1039/C8TA08248K>.
- [39] C. Manière, G. Lee, E.A. Olevsky, Proportional integral derivative, modeling and ways of stabilization for the spark plasma sintering process, *Results Phys.* 7 (2017) 1494–1497. <https://doi.org/https://doi.org/10.1016/j.rinp.2017.04.020>.
- [40] E. Alleno, D. Bérardan, C. Byl, C. Candolfi, R. Daou, R. Decourt, E. Guilmeau, S. Hébert, J. Hejtmanek, B. Lenoir, P. Masschelein, V. Ohorodnichuk, M. Pollet, S. Populoh, D. Ravot, O.

Rouleau, M. Soulier, Invited Article: A round robin test of the uncertainty on the measurement of the thermoelectric dimensionless figure of merit of  $\text{Co}_{0.97}\text{Ni}_{0.03}\text{Sb}_3$ , *Rev. Sci. Instrum.* 86 (2015) 11301. <https://doi.org/10.1063/1.4905250>.

- [41] A.C. Larson, R.B. Von Dreele, General Structure Analysis System (GSAS), Los Alamos Natl. Lab. Rep. LAUR 86-748. (1994).
- [42] B. Toby, EXPGUI, a graphical user interface for GSAS, *J. Appl. Crystallogr.* 34 (2001) 210–213. <https://doi.org/10.1107/S0021889801002242>.